

Laser compression of monocrystalline tantalum

C.H. Lu^a, B.A. Remington^b, B.R. Maddox^b, B. Kad^a, H.S. Park^b, S.T. Prisbrey^b,
M.A. Meyers^{a,*}

^a University of California, San Diego, La Jolla, CA 92093, USA

^b Lawrence Livermore National Laboratory, Livermore, CA 94550, USA

Received 31 May 2012; received in revised form 9 August 2012; accepted 14 August 2012

Available online 19 September 2012

Abstract

Monocrystalline tantalum with orientations [100] and [111] was subjected to laser-driven compression at energies of 350–684 J, generating shock amplitudes varying from 10 to 110 GPa. A stagnating reservoir driven by a laser beam with a spot radius of ~800 μm created a crater of significant depth (~80 to ~200 μm) on the drive side of the Ta sample. The defects generated by the laser pulse were characterized by transmission and scanning electron microscopy, and are composed of dislocations at low pressures, and mechanical twins and a displacive phase transformation at higher pressures. The defect substructure is a function of distance from the energy deposition surface and correlates directly with the pressure. Directly under the bottom of the crater is an isentropic layer, approximately 40 μm thick, which shows few deformation markings. Lattice rotation was observed immediately beneath this layer. Further below this regime, a high density of twins and dislocations was observed. As the shock amplitude decayed to below ~40 GPa, the incidence of twinning decreased dramatically, suggesting a critical threshold pressure. The twinning planes were primarily {112}, although some {123} twins were also observed. Body-centered cubic to hexagonal close-packed pressure induced-transformation was observed at high pressures (~68 GPa).

The experimentally measured dislocation densities and threshold stress for twinning are compared with predictions using analyses based on the constitutive response, and the similarities and differences are discussed in terms of the mechanisms of defect generation. © 2012 Acta Materialia Inc. Published by Elsevier Ltd. All rights reserved.

Keywords: Dislocation; Laser treatment; Tantalum; Twinning; Shock compression

1. Introduction

Although the first laser shock experiments, by Askaryan et al. [1], date from the 1960s, and early work showed the potential use of laser shock pulses to harden aluminum alloys [2,3], there has been only limited inquiry on the nature of laser-shock-induced defects. White [4,5] and others [6–8] introduced the use of lasers to obtain Hugoniot data over a broad range of pressures.

A systematic inquiry into the effects of laser pulses on fcc metals (Cu and Cu–Al) was initiated in 2001 and has yielded significant results that have been explained in terms

of shock compression [9–11]. This work was extended to nickel by Jarmakani et al. [12].

The objective of this study is to extend the methodology developed for copper and nickel to a model body-centered cubic (bcc) metal, tantalum. There are important fundamental differences between face-centered cubic (fcc) and bcc metals; in tantalum, the Peierls–Nabarro stress is ~2.97 GPa [13], whereas it is only ~19 MPa in copper [14]. This difference profoundly affects the temperature and strain-rate sensitivities, and is expressed in different constitutive equations developed by Zerilli and Armstrong [15]. Tantalum has been subjected to shock compression experiments using gas-gun [16] and explosively driven flyer plate techniques [17]. The slip–twinning transition has been observed [18,19], and the bcc–hexagonal close-packed

* Corresponding author. Tel.: +1 858 534 4719.

E-mail address: mameyers@ucsd.edu (M.A. Meyers).

(hcp) transformation was identified by Hsiung [20] and Hsiung and Lassila [21,22].

The dislocation response is governed at low strain rates by thermal activation. With increasing strain rate, drag (phonon and electron) mechanisms become relevant [23], as well as a proposed new regime of effective “drag” through debris generation [24]. At even higher strain rates, relativistic effects have been postulated.

In spite of extensive research, we still do not fully understand at the lattice level how a strong shock – that is, a shock where the plastic wave has a higher shock velocity than the elastic precursor – propagates through a solid sample [9]. Further, the timescale and physical processes involved in elastic–plastic [25] and polymorphic phase transitions [26] are fertile areas of investigation.

The regimes obtained by laser-induced compression are extreme and cannot be accessed by other experimental methods. The timescales are two to three orders of magnitude shorter than those in gas-gun and explosive experiments. The goal of this research is to probe the mechanisms of plastic deformation (slip and twinning) in a time and pressure region accessible via laser energy deposition. Recovery experiments of ramp-loaded, monocrystalline Ta were designed to study mechanisms of plastic deformation and failure at high pressure and strain rates.

2. Experimental techniques

Pure monocrystalline Ta was obtained from MarkeTech Intl, Inc. in cylindrical shape, with dimensions of 3 mm diameter and 3 mm height. The interstitial impurities (ppm in weight) in Ta measured by the Evans Analytical Group are O:<10, N:<10, H: 7.6 and C:<10. The laser recovery experiments were performed at the Laboratory for Laser Energetics, University of Rochester (Omega Facility). The experimental set-up, shown in Fig. 1, had previously been tested for recovery of fcc metals [9]. The cylindrical tantalum monocrystal targets were placed behind a tantalum washer inside a stainless steel recovery container. The inside of this container was filled with silica aerogel, which acted as a deceleration medium for the tantalum specimens after they had undergone compression loading.

The recovery container was designed to be mounted in the Omega chamber [27,28] (Fig. 1a). Fig. 1b shows a more detailed view of the recovery set-up. A shock was driven into the 180 μm BrCH (2%) reservoir via direct illumination of the 20 μm polycarbonate ablator by six overlapping beams at a nominal energy of ~ 60 J per beam for ~ 3 ns. The standard SG8 distributed phase plates (focal spot of radius ~ 400 μm) were used [29] on each beam, with best focus at the ablation surface. The overlap region between the six beams was optimized to ensure a large, uniform ablation front. The stagnation of the reservoir material against the Ta sample provided a quasi-isentropic loading profile for a few tens of micrometers of Ta sample before steepening into a shock [30]. The detailed cross-section of

the target holder with the tantalum specimen to be studied is shown in Fig. 1c. The specimens were successfully recovered in this geometry. The aerogel did not introduce any additional damage into the recovered samples and acted as a gradual decelerating medium. A removable cap with a centered 4 mm hole was used to clamp and fix the sample at the front end of the tube (Fig. 1a).

The generation of shockless compression using an expanding plasma has three stages. First, the incident laser energy flux is converted in the ablator/reservoir into a low-density plasma [27]. Secondly, the plasma expands in the gap. Thirdly, the plasma stagnates and piles up against the front surface of the tantalum, producing a monotonically rising pressure. The amplitude of the pressure wave propagating into the monocrystal increases and gradually steepens into a shock wave as it propagates into the metal. Surface heating effects are minimized through this process. A 3 mm diameter and 20 μm thick polycarbonate ablator ($\text{C}_{16}\text{H}_{16}\text{O}_4$), density 1.2 g cm^{-3} , followed by 180 μm thick brominated polystyrene reservoir ($\text{C}_{50}\text{H}_{48}\text{Br}_2$), density 1.23 g cm^{-3} , was placed on the laser-irradiating front surface of the tantalum washer (Fig. 1c). The Ta washer, with a machined radial groove for vacuum pumping of the gap (marked in Fig. 1c), was clamped between the cap and the front end of the tube. The radial groove was designed for pumping out the gap between the ablator/reservoir and the front surface of monocrystals. The internal diameter of the Ta washer is 2 mm, determining the diameter of the compression pulse.

Five recovery experiments on monocrystals and three complementary VISAR (Velocity Interferometer System for Any Reflector) experiments of the drive were performed. The VISAR experiments were conducted on Al–LiF drive calibration samples and provided interface velocity data that allowed the pressure vs. time of loading to be deduced, which became the input to the subsequent computer simulations. The total drive laser energies (E_{Laser}) varied between 350 and 684 J.

The shocked targets were examined using a profilometer, a microhardness tester, a scanning electron microscope (Phillips XL30 ESEM) and transmission electron microscopes (operated at 200 kV). Transmission electron microscopy (TEM) foils were prepared by electropolishing and focused ion beam (FIB; Hitachi NB-5000 FIB-SEM) techniques. The electropolishing liquid was a solution of 87.5 vol.% methanol, 10 vol.% sulfuric acid and 2.5 vol.% hydrofluoric acid, which was used to polish at ~ 25 V and ~ -35 °C. The temperature was lowered by pouring liquid nitrogen directly into the electropolishing solution. FIB samples were prepared by cutting targets into half along the energy deposition direction and mounting them into epoxy. They were mechanically polished down to 0.05 μm using Al_2O_3 and coated with a thin layer of Ir before the FIB milling procedure. The FIB samples were perpendicular to the shock propagation direction and had thicknesses of 50–100 nm. DIFFRACT™ was used to simulate the diffraction patterns taken from TEM images.

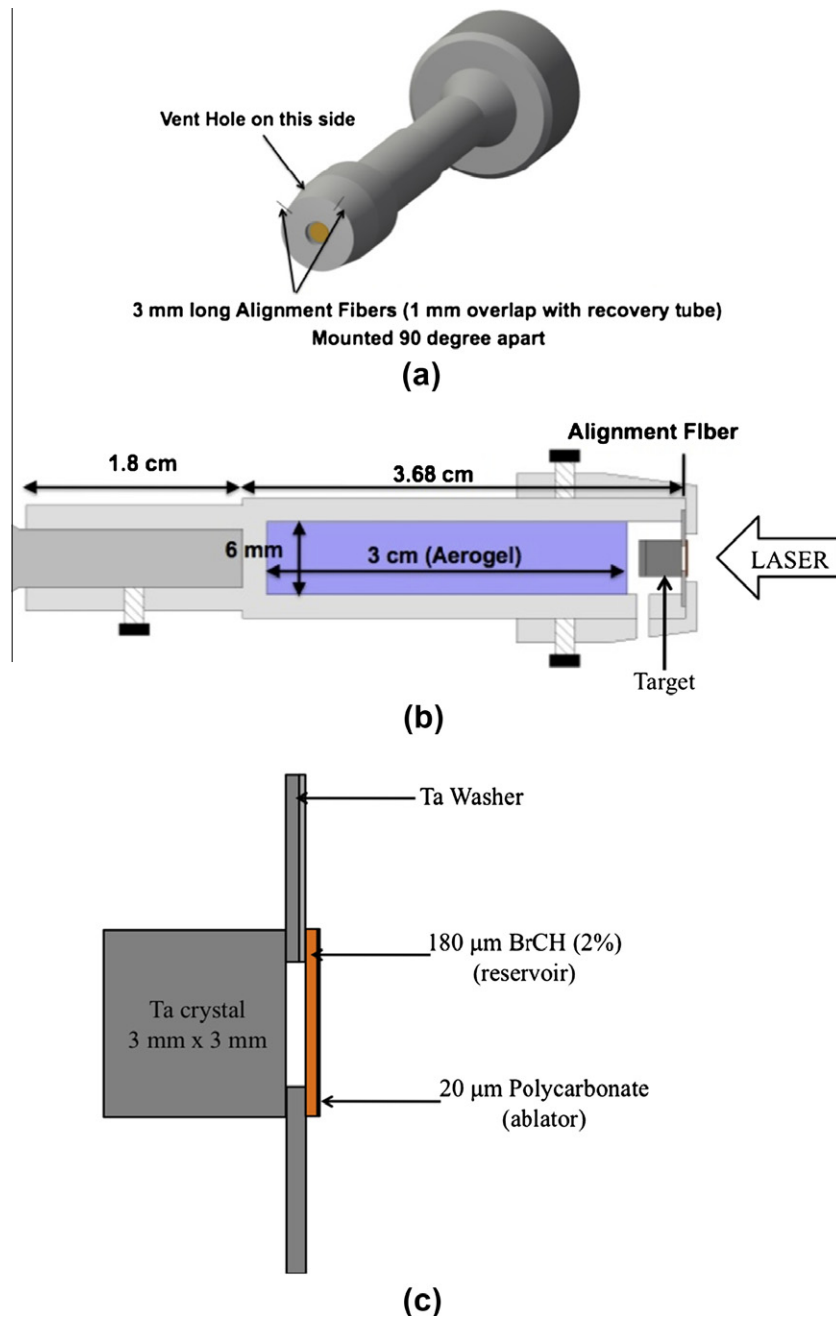


Fig. 1. (a) Tridimensional illustration of recovery tube; (b) cross-section of the recovery tube with dimensions; (c) detailed cross-section of the laser package and recovery tantalum specimen.

3. Results and discussion

3.1. SEM analysis

The laser-driven loading produced significant cratering of the specimen surfaces. Figs. 2 and 3 show the craters, their profiles and scanning electron microscopy (SEM) observations of the surfaces for [100] and [111] monocrystals at the lowest (~ 350 J) and highest (~ 684 J) drive laser energies, respectively. The crater radius is ~ 1.2 mm in all cases, but the depth is a function of the laser energy, being

approximately 0.08 mm for the 350 J and ~ 0.21 mm for the 684 J total laser energy. Fig. 4 shows plots of the crater dimensions vs. laser energy; the crater depth increases monotonically with laser energy (Fig. 4a), whereas the crater radius is largely independent of it (Fig. 4b).

The SEM micrographs of the shocked specimens reveal interesting features. First, the “blow-off” effect from the laser energy deposition is seen through striations that emanate from the central region. This “blow-off” likely involves melting of the surface layers. SEM micrographs also show other features of relevance: two arrays of perpen-

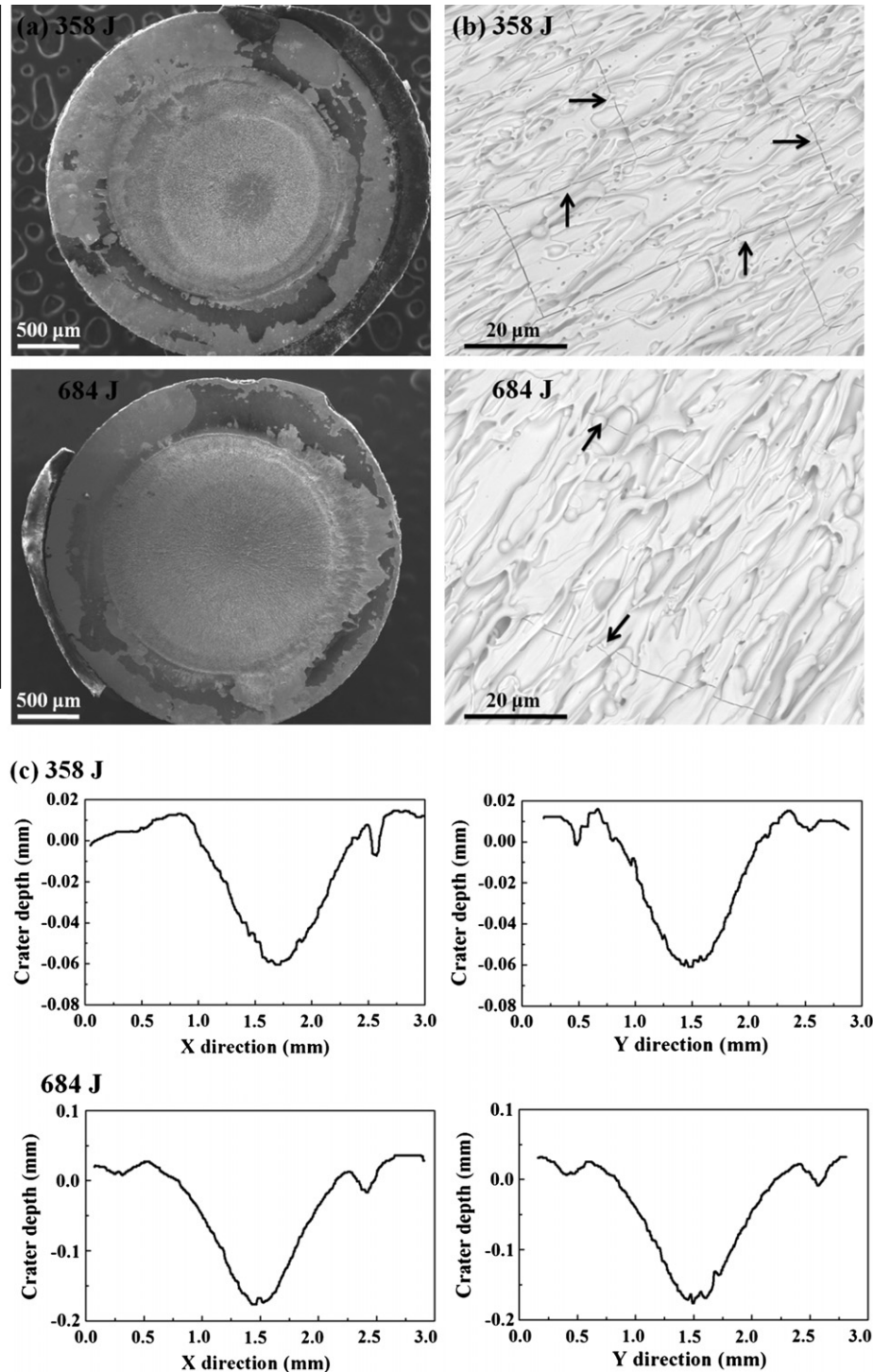


Fig. 2. Surface of Ta [100] monocrystals after laser compression (top: $E_{\text{Laser}} = 358$ J; bottom: $E_{\text{Laser}} = 684$ J). (a) Optical micrographs; (b) SEM showing cracks; (c) profilometry traces.

dicular dark lines (marked by arrows) are seen in the [100] crystal (Fig. 2). These lines are also present in the [111] crystal, but are irregular. Two possibilities were considered: cracks and twins. The irregular lines in the [111] crystal (Fig. 3) are not consistent with twin traces. It is possible that bcc tantalum undergoes a ductile-to-brittle transition at high strain rates, where the cracks could be formed in

tension generated by the large stress, temperature and deformation gradients generated by the laser pulse. Ductile-to-brittle transitions in bcc metals due to temperature effects have been studied both experimentally [31,32] and computationally [33], but high strain rate effects are not as well understood as temperature effects. However, the two effects, lowering the temperature and increasing the

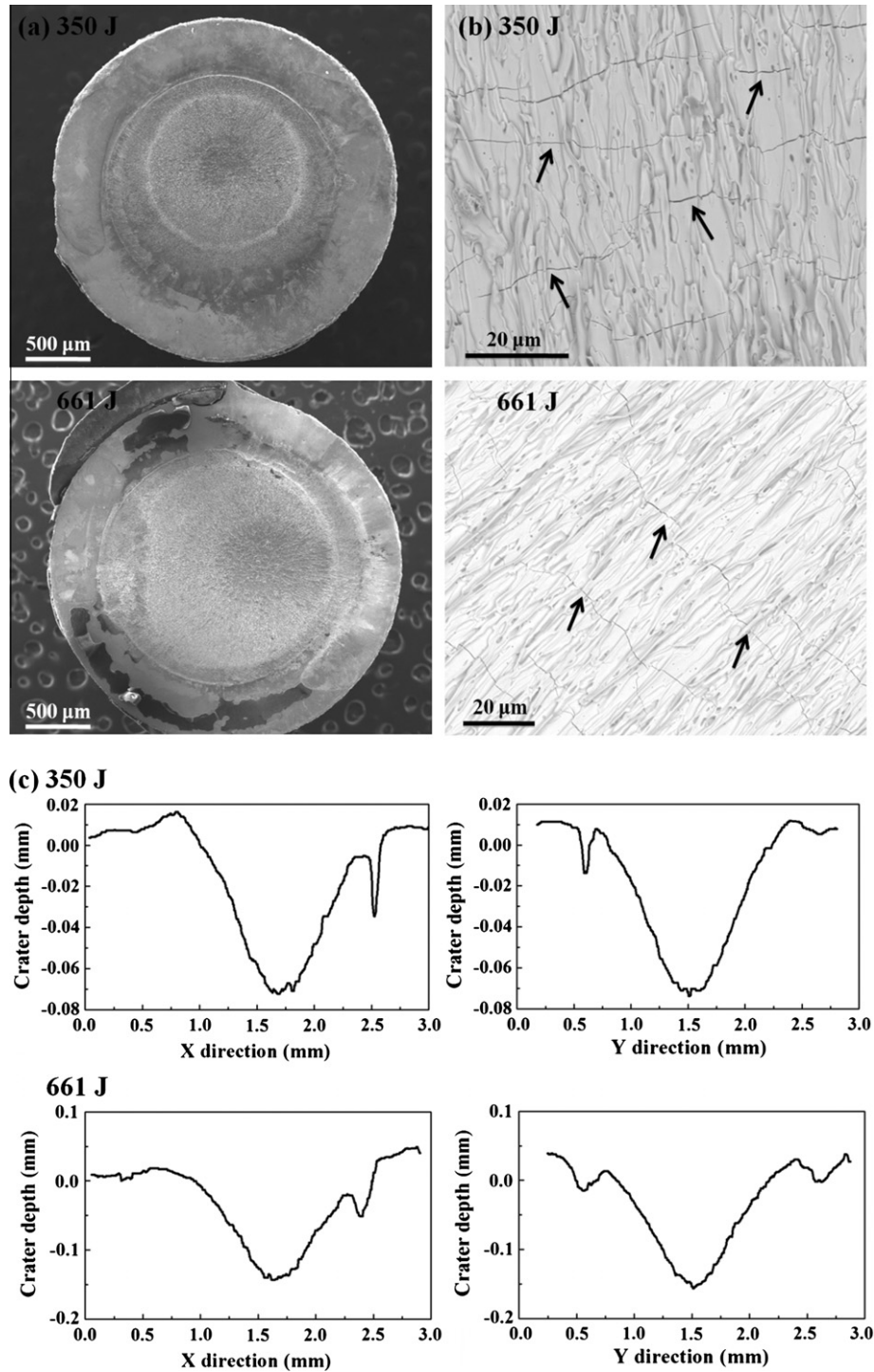


Fig. 3. Surface of Ta [1 1 1] monocrystals after laser compression (top: $E_{\text{Laser}} = 350$ J; bottom: $E_{\text{Laser}} = 661$ J). (a) Optical micrographs; (b) SEM showing cracks; (c) profilometry traces.

strain rate, restrict dislocation motion and promote brittle fracture.

3.2. VISAR analysis

The initial pressure pulse was calibrated using the VISAR traces of the Al–LiF witness plate interface velocity

obtained from independent experiments under similar laser energy conditions. Fig. 5a shows the superimposed VISAR (dashed line) and LASNEX simulations (full line) traces. To obtain a good fit, the initial LASNEX computed energy was corrected by a factor of 0.7 to account for two-dimensional effects in a one-dimensional simulation. Tabulated measured/calculated electron thermal conductivity values

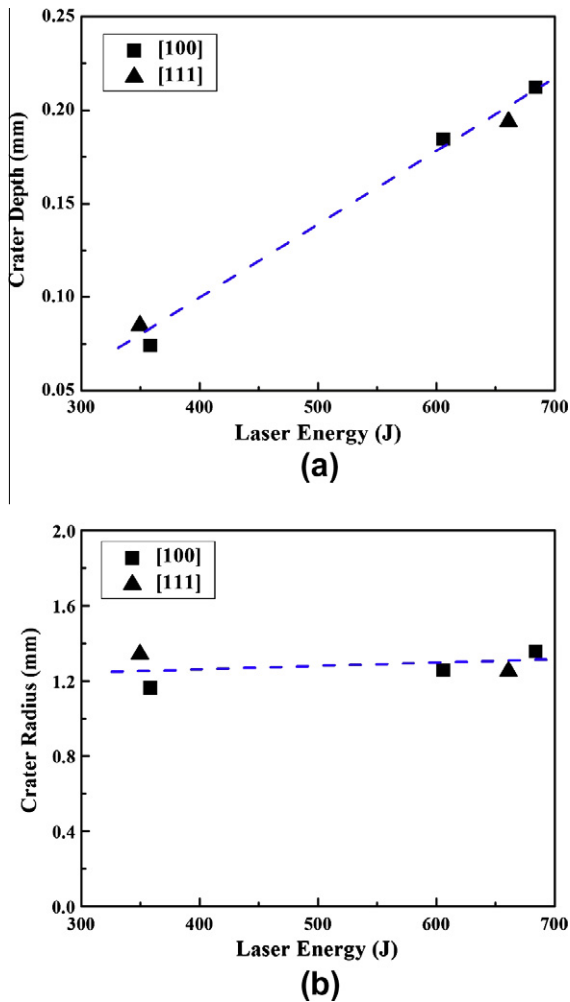


Fig. 4. (a) Depth and (b) radius of craters formed in [100] and [111] monocrystals as a function of laser energy. No significant differences in crater radius between the [100] and [111] samples are observed.

were used. In spite of using a polycarbonate ablator/reservoir, heating of the front of the Ta sample still occurs due to the high-energy photon deposition into the Ta sample during laser ablation and the diffusion process used to model radiation propagation in the simulation. An aspect of the experimental set-up that is of relevance is that the initial pulse rise is not a shock discontinuity. This is seen in Fig. 5b; the temperature is expressed as eV ($\sim 12,000$ K). For distances of 5 and 10 μm from the energy deposition surface, the quasi-isentropic loading condition prevails, providing a gradual temperature rise. By the time the stress wave has penetrated 50 μm into the sample, the temperature rise is much more rapid. This quasi-isentropic loading was purposely incorporated into the target design to minimize the temperature rise at high pressures. The dip in T_{ion} just before ramp occurs is due to the transition of the zonal region from elastic to plastic flow and is an artifact of the simulation (not real). The ion temperature after the transition to plastic flow is still valid and can be seen to be ramp-like in nature until the sample is ~ 25 –30 μm in thickness. Then the induced shock heating caused

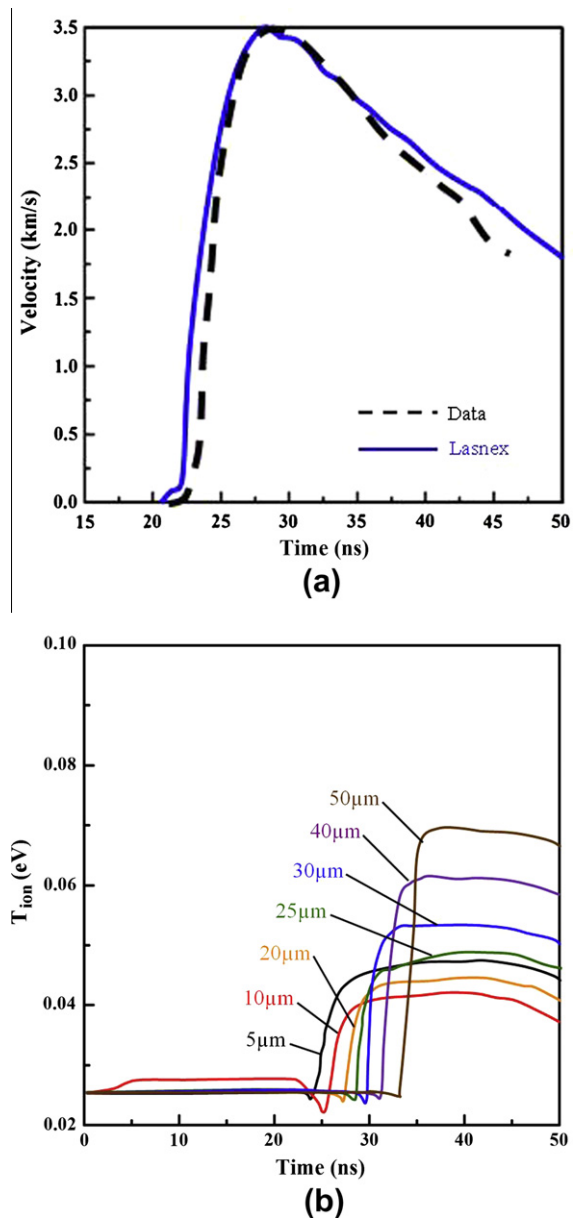


Fig. 5. Measured and simulated parameters for laser energy of $E_{\text{Laser}} = 684$ J: (a) measured VISAR and simulated LASNEX traces of the Al–LiF interface velocity from a drive shot; (b) 1D LASNEX simulation of temperature as a function of time at different depths into the Ta. Note the transition from quasi-isentropic to shock compression with an attendant decrease in rise time and increase in temperature (12,000 K, ~ 1 eV).

by the steepening of the ramped compression wave into a shock causes an abrupt jump in T_{ion} and the ramp-like nature is lost.

Fig. 6 shows the calculated pressure decay using the LASNEX radiation hydrodynamics code with the assumption of one-dimensional propagation. The radial release is not incorporated into the calculation, which is reasonable for a depth of up to 2 mm in our experimental set-up. The pressure–time profiles at different depths are shown in Fig. 6a and b for E_{Laser} of 358 and 684 J, respectively. The pressure decays rapidly, but is still significant at the

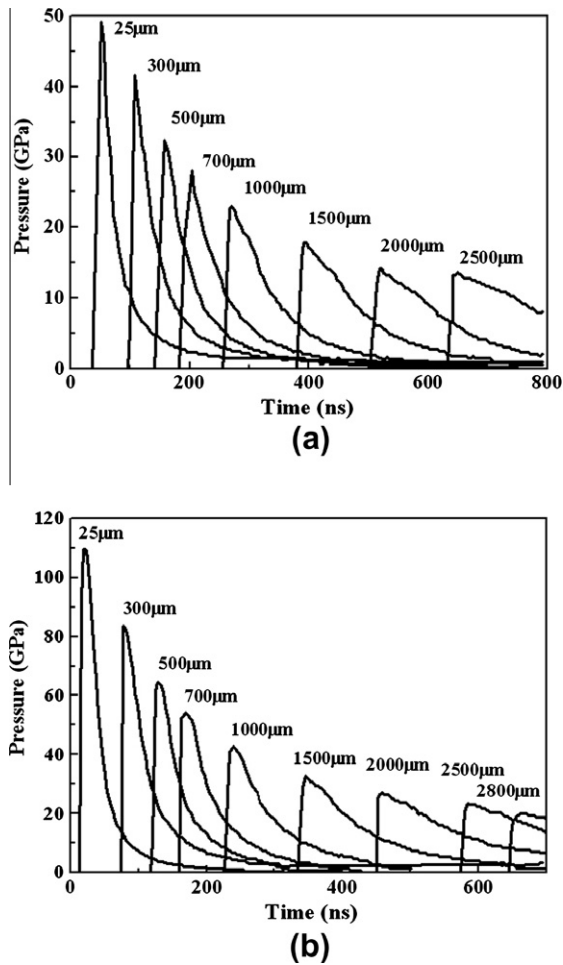


Fig. 6. LASNEX simulations of the decay of the laser-generated pressure pulse as it travels through tantalum specimen for (a) total laser energy of 358 J and (b) total laser energy of 684 J.

back surface of the specimen (3 mm). At the same time, the pulse, which has a characteristic triangular shape, widens with depth into the sample. At each depth, the largest pressure occurs along the energy deposition axis and is indicated as “peak pressure” at that depth. For the $E_{\text{Laser}} = 358$ J (Fig. 6a) experiment, the pressure decays from ~ 50 to ~ 10 GPa from the front (loading side) to the back of the sample. For the $E_{\text{Laser}} = 684$ J (Fig. 6b) experiment, it decays from ~ 110 to ~ 20 GPa.

3.3. Microhardness analysis

The shocked and recovered [100] and [111] specimens were sectioned into six slices along their 3 mm length (Fig. 7a), slice 1 being ~ 600 μm thick and the other slices ~ 250 μm thick (Fig. 7a). After brief mechanical polishing of all flat surfaces, microhardness values were measured across the diameter of each slice. The microhardness varies across the sample diameter, being highest in the center due to the localization of the laser pulse in the central portion of the specimens (Fig. 7b). The microhardness of the [100] crystal driven with $E_{\text{Laser}} = 606$ J as a function of dis-

tance from the driven Ta surface is shown in Fig. 7c. The microhardness decays from the front to back, from ~ 1500 to ~ 900 MPa. This decay is most significant in the first millimeter from the compression surface. The original microhardness (before laser compression) is ~ 760 MPa. The dashed line shows a hardness discontinuity, related to the slip-to-twinning transition, as explained in Section 3.4. The microhardness was also measured in the slices for the $E_{\text{Laser}} = 358$ and 684 J experiments; the corresponding positions were converted to the respective pressures through the use of the LASNEX calculations of Fig. 6. For the 606 J experiment, the pressures were interpolated from the 358 and 684 J simulations. The relation between microhardness and pressure is shown in Fig. 7d. By assessing the slice location, we can extract the pressure from Fig. 6. It can be seen that the results from the three experiments are consistent. These results do not follow the Murr expression, $H \propto P^{1/2}$ [34]. This is due to the fact that twinning is prevalent above $P \sim 43$ GPa, as marked in Fig. 7d. The onset of twinning in Ta has been shown by Murr et al. [19] to generate an increase in hardness, as evident from our results.

3.4. TEM analysis

3.4.1. Dislocation density analysis

TEM foils for dislocation density analysis were prepared by electropolishing slices 2–6 (see Fig. 7a) for the [100] monocrystals. TEM characterization shows the deformation structures associated with the passage of the pressure wave/shock. Typical deformation substructures are shown in Fig. 8. The dislocation density decreases with distance from the laser deposition surface. The dislocation segments are predominantly of screw character, a feature well known in bcc metals since the edge dislocations have much higher mobility. As pressure increases (Fig. 8a), the dislocations tend to organize into well-defined bands. The $g = 200$ imaging condition in Fig. 8a is normal to the deformation band, consistent with the projected (101) slip trace in bcc tantalum.

Fig. 9b shows a high magnification region of loops observed in slice 3 of the [100], $E_{\text{Laser}} = 358$ J sample. This is compared with earlier work on laser-shocked copper (Fig. 9a). There are striking similarities in loop structure between the laser-shocked Cu and Ta. The presence of large numbers of dislocation loops has been previously identified by Meyers et al. [9]. Similarly, tantalum shows the same proclivity for shear loop formation as marked in Fig. 9b.

3.4.2. Twin structure analysis

The FIB technique was used to prepare TEM foils from slice 1 (Fig. 7a), for the locations just below the energy deposition surface at the center of the crater. The removal of FIB foils from slice 1 of the Ta [001] with $E_{\text{Laser}} = 606$ J is shown in Fig. 10a. The foil “Top” comes from 54 μm beneath the center of the crater bottom, whereas the foil

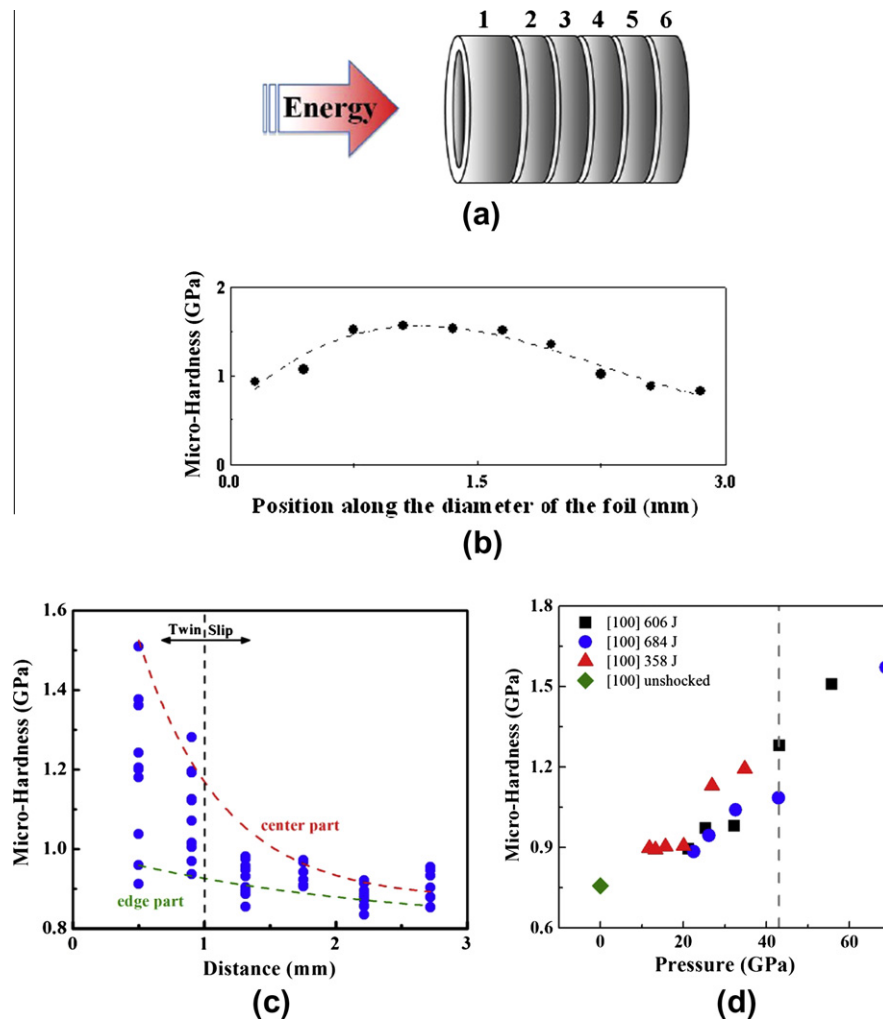


Fig. 7. (a) Slices into which the specimens were cut: slice 1 was $\sim 600 \mu\text{m}$, slices 2–6 $\sim 250 \mu\text{m}$ thick before polishing. (b) Microhardness variation along diameter for slice 1 of [100] crystal, total laser energy of 684 J. (c) Microhardness variation in [100] crystal as a function of depth, total laser energy of 606 J. At each depth (slice), the microhardness values were measured across the slice diameter. The “center part” dashed line corresponds to the crater center axis, while the “edge part” corresponds to the edge of each slice. The vertical dashed line indicates the approximate position of the slip–twin transition boundary. (d) Combined results for center part microhardness in a [100] crystal as a function of shock pressure. When pressure exceeds a threshold value, indicated by the dashed line, twinning is observed.

“Bottom” comes from 202 μm below the crater bottom. The foil “Edge” comes from the same depth from the energy deposition surface as foil “Top” but close to the edge of the target, as shown in Fig. 10a. The thickness of the FIB sample is about 50–100 nm. There are only small grains [35] observed in the top foil (Fig. 10b), while abundant deformation substructures are observed in the bottom foil (Fig. 10c). Comparing the top and edge foils, the grains in top foil rotated $\sim 14.8^\circ$ off the [001] zone axis. Dark-field images using selected diffraction spots (marked by arrow) are shown in Fig. 10c. They reveal substructures in three crystallographic directions. A software simulation result consistent with the experimental diffraction pattern is shown in Fig. 11.

The diffraction pattern with foil normal [001] and zone axis = [103] is shown in Fig. 11a by black diffraction spots. The $\{112\}$ bcc twin plane and $\langle 111 \rangle$ directions were used to simulate twin spots. Therefore, the additional diffraction

spots for twinning structures in this monocrystalline Ta foil with zone axis tilted less than 0.1° toward the $[0\bar{1}3]$ axis are shown in Fig. 11a (open circle diffraction spots). In comparison with the experimental results (Figs. 10c and 11b), the twinning structures induced by laser shock compression in monocrystalline [001] Ta can be identified; the twin planes are $(\bar{1}21)$, $(\bar{2}11)$ and $(\bar{1}21)$.

Shock compression-induced twinning has been previously identified by several investigators. Murr et al. [19] observed it in polycrystalline tantalum ($\sim 43 \mu\text{m}$ grain size) at ~ 45 GPa. There was significant twinning, which was dependent on grain orientation, and this resulted in additional hardening in post-shock quasi-static testing. Gray and Vecchio [36] shocked polycrystalline tantalum ($\sim 68 \mu\text{m}$ grain size) to ~ 20 GPa and also observed twinning. However, they report that only a limited amount of twinning was observed and that the subsequent quasi-static stress–strain response was not affected. Thus, one can

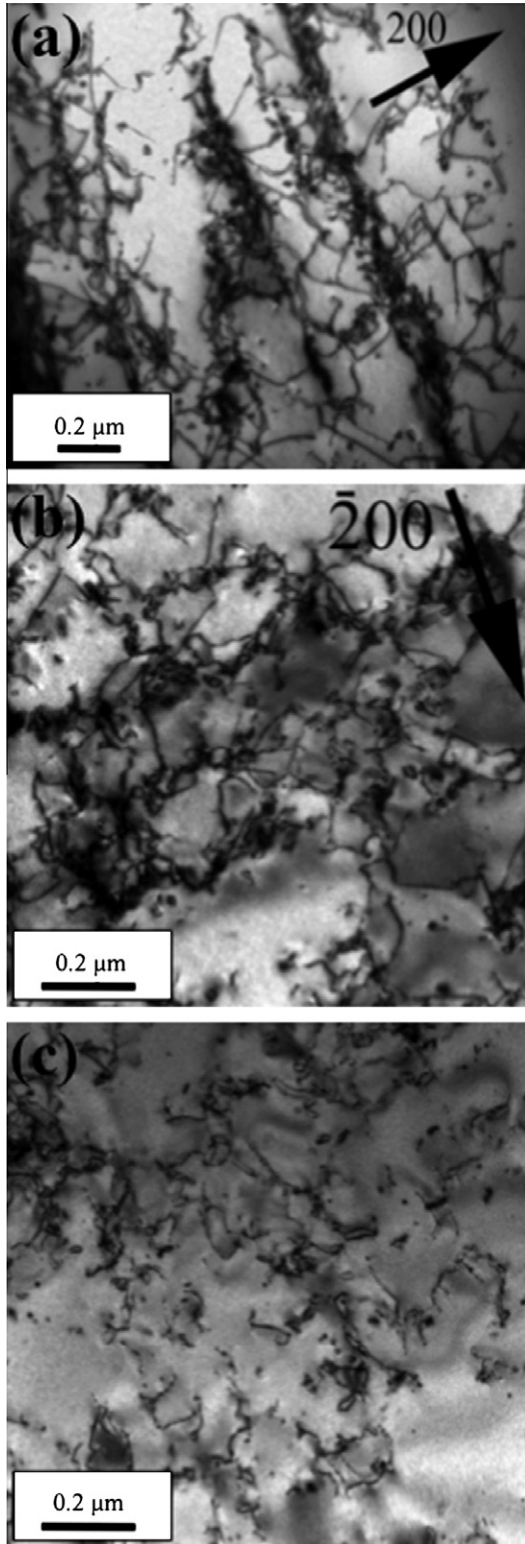


Fig. 8. TEM micrographs as a function of distance from the laser deposition surface for a [001] Ta single crystal, driven with laser energy of 606 J: (a) slice 3 (1.3 mm from laser impact surface; local pressure ~ 32.2 GPa); (b) slice 5 (2.2 mm from laser impact surface; local pressure ~ 21.2 GPa); (c) slice 6 (2.7 mm from laser impact surface; local pressure ~ 18.8 GPa). Foil normal $\cong [001]$. All images were taken with two electron beam conditions $\sim 5^\circ$ off [001] in the transmission electron microscope. The micrographs show dislocation tangles from deformation by slip, but no obvious evidence of twinning.

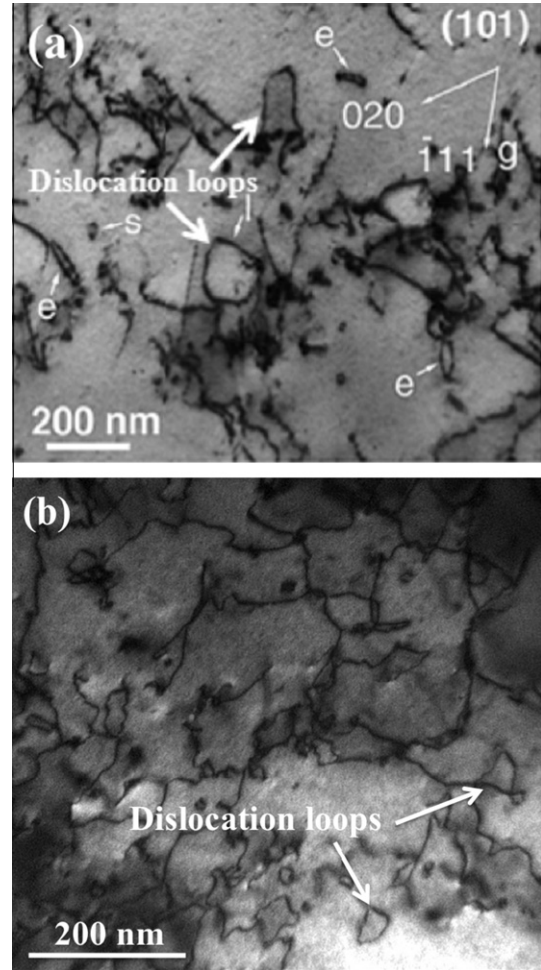


Fig. 9. Dislocation loops in shocked (a) monocrystalline copper [9] and (b) monocrystalline tantalum at a laser energy of 358 J and average pressure of ~ 22 GPa (slice 3).

consider 20 GPa as a lower bound for twinning in polycrystalline Ta. Hsiung [20] and Hsiung and Lassila [22] observed twins in pure Ta at 45 GPa but not at 30 GPa. In our current study, twinning structures were observed to depths of slice 2 in [001] driven at $E_{\text{Laser}} = 606$ J and of slice 3 in [001] driven at $E_{\text{Laser}} = 684$ J (Fig. 12). We estimate the pressure for slice 3 in [001] driven at $E_{\text{Laser}} = 684$ J to be ~ 32 GPa (from Fig. 6b), at a depth of ~ 1.49 mm from the front surface for this slice. Similarly, we estimate the pressure for slice 2 in [001] driven at $E_{\text{Laser}} = 606$ J as 43 GPa, interpolated for its 0.9 mm depth from the front surface. The slip–twinning transition is likely somewhere between 32 and 43 GPa in pure Ta, consistent with Murr et al. [19] and Hsiung [20]. It should be mentioned that twins and dislocations are generated not by the pressure, but by the shear stresses associated with compression in uniaxial strain. This will be discussed in greater detail in Section 3.5.2.

Murr [34] reports an increase in hardness associated with the formation of twins. This is also seen in Fig. 7c. There are two lines in Fig. 7c – one at the edge and one

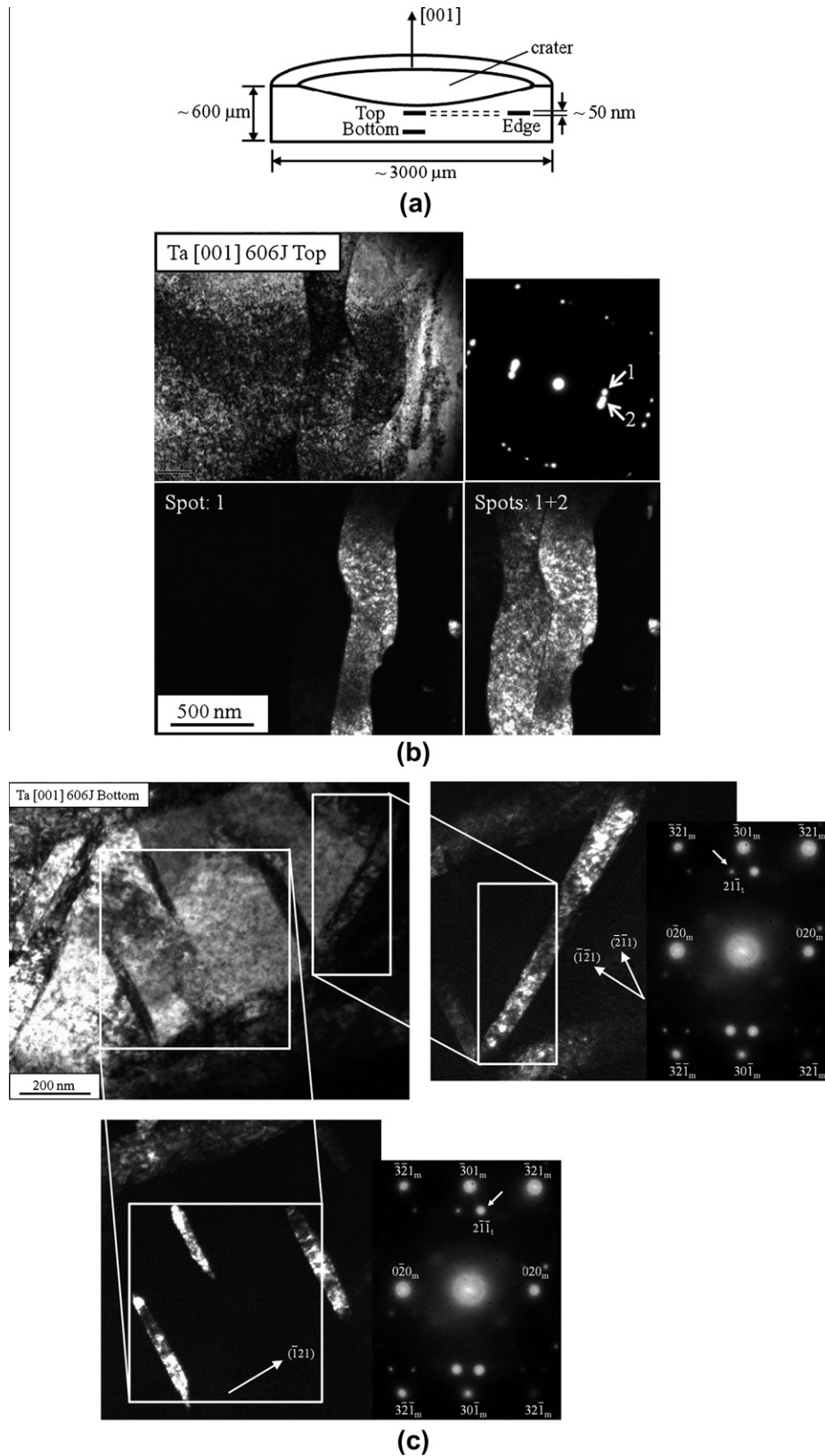


Fig. 10. (a) FIB cutting location in slice 1 for [001] orientation of Ta at $E_{\text{Laser}} = 606$ J. “Top” foil: ~ 50 μm from the crater bottom (~ 78 GPa); “Bottom” foil: ~ 200 μm from the crater bottom (~ 68 GPa). “Edge” foil: the same depth as “Top” foil, but far away from the crater center. (b) TEM bright-field images and diffraction pattern of “Top” foil; (c) dark-field images and selected diffraction patterns in the “Bottom” foil. Foil normal $\cong [103]$. The beam conditions were $\sim 5^\circ$ off [103] in the transmission electron microscope.

at the center – indicating that the results come from the central axis and outer edge of the cylindrical monocrystal, respectively. The vertical dashed line in Fig. 7c marks a discontinuity in hardness and corresponds to the TEM observations of twins. This line is ~ 1 mm from the front for $E_{\text{Laser}} = 606$ J. Similarly, it is ~ 1.5 mm from the front for $E_{\text{Laser}} = 684$ J. In all cases, the discontinuity in hardness occurs at a pressure of ~ 30 – 40 GPa (Fig. 7d).

Looking back to the isentropic deformation profile, described in Section 3.2, the examination of the deformation substructure in the region just below the surface is of importance. For this reason, the front and back surfaces of slice 1 for $E_{\text{Laser}} = 606$ J were simultaneously evaluated via surface and backscattered SEM techniques. It should be noted that the front and back surfaces of slice 1 are at depths of ~ 186 and ~ 600 μm , respectively. Sample surfaces were slightly electropolished for ease of examination, and the depth of metal removed was carefully tracked via profilometry. Successive polishing, profilometry and SEM yielded the deformation substructure as a function of depth. On the first iteration, no substructure was observed on the front surface but extensive substructures are revealed on the back surface of slice 1 for $E_{\text{Laser}} = 606$ J, as shown in Fig. 13a and c. Because of the extreme deformation gradient, evidenced by the variance of surface features on the front and the back face of slice 1 for $E_{\text{Laser}} = 606$ J, it was necessary to incrementally polish and explore the depth-dependent deformation substructure. After repeated surface removal steps by electropolishing, profuse twinning is first observed in only one small part on the front surface of slice 1 at a depth of ~ 42 μm from the crater surface (Fig. 13b). It is thus surmised that the extent of the isentropic layer is of the order of ~ 40 μm . This is also consistent with the simulation results shown in Fig. 5b. However, the absence of features can also be due to thermal annealing.

The orthogonal deformation twins observed in back-scattered SEM (Fig. 13b and c) are marked by arrows A, B and C, D. The nominal spacing is about 0.5 μm and the thickness is, at most, ~ 0.2 μm . Fig. 13d shows profuse twinning patterns observed via TEM. The orthogonal pattern of twins observed is also marked by arrows A and B. These correspond to the traces of $\{112\}$ of the slip systems with a Schmid factor of 0.457 on the (001) plane of the foil. There is also a significant number of markings at $\sim 40^\circ$, marked C and D. These are likely traces of the $\{123\}$ slip planes [37], with the highest Schmid factor (0.463) on the (001) plane of the foil. Therefore the $\{112\}$ and $\{123\}$ slip systems are activated under almost similar conditions.

3.4.3. BCC to HCP transformation

The detailed mechanism of the α (bcc) $\rightarrow \omega$ (hexagonal) phase transformation in Ta was proposed by Hsiung [20] following experimental observations and confirmation via simulation. For monocrystalline Ta ($[011]$ orientation), the shock-induced ω -phase transformation was observed at 45 GPa but not at 15 GPa [22]. In the current research, the ω -phase was observed for $[001]$ at $E_{\text{Laser}} = 606$ J in the foil “Bottom” and is shown in Fig. 14. From LASNEX simulation results, the peak pressure of the foil “Bottom” in slice 1 (202 μm under the crater bottom) is ~ 68 GPa. However, there are only twinning structures, in slice 2 of the same target, at a peak pressure ~ 43 GPa. The Schmid factor of the transformation plane and direction ($\{211\}\langle 111\rangle$) is higher for $[011]$ than for $[001]$ loading. Thus, to a first approximation, the transformation pressure for $[011]$ loading should be lower than for $[001]$. Similar to the experimental results from Hsiung [20] and Hsiung and Lassila [22], the ω -phase is bulky (Fig. 14) compared to the lenticular shape of the twin structure (Figs. 10c and 12). The phase transition threshold pressure seems to be higher than the slip–twinning transition pressure.

3.5. Modeling

3.5.1. Dislocation densities: comparison with experimental results

Two analyses are applied in this section: the first is the mechanism for homogeneous dislocation generation behind the shock front [38,39]; the second is dislocation multiplication by the Orowan mechanism. They yield quantitative predictions of dislocation densities which are compared with experimental results obtained here and those reported by Hsiung [20] and Gray and Vecchio [36]. The dislocation density ρ can be statistically calculated from the TEM pictures through:

$$\rho = \frac{2\bar{N}}{Lt}$$

where \bar{N} is the number of intersections on a grid line L , and t is the thickness of the sample [40–42]. From the FIB technique, we approximate the thickness of the TEM samples as 50 nm. Using the relation between pressure and depth

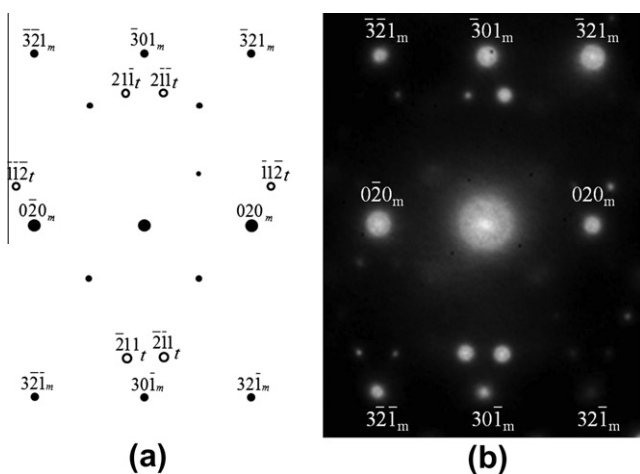


Fig. 11. (a) Diffraction pattern simulated by DIFFRACT™ as foil normal = $[001]$ and zone axis = $[103]$ with zone axis tilted less than 0.1° toward $[0\bar{1}3]$ axis (subscripts m and t denote matrix and twin, respectively). (b) Experimental diffraction pattern from FIB foil “Bottom”; 202 μm below the crater bottom.

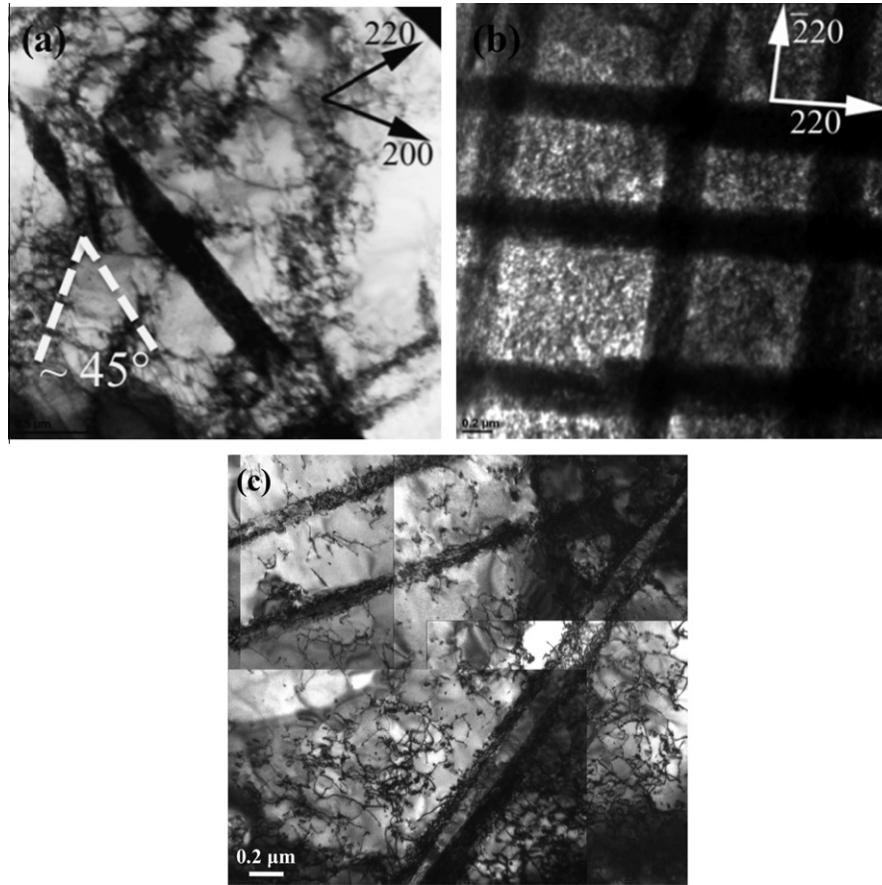


Fig. 12. Mechanical twinning induced by laser compression (a and b) at 0.9 mm from the drive surface (slice 2) for the [100] orientation of Ta at $E_{\text{Laser}} = 606$ J, corresponding to an average shock strength of ~ 43 GPa; (c) at 1.49 mm from the driven surface (slice 3) for the [100] orientation of Ta at $E_{\text{Laser}} = 684$ J, corresponding to average shock strength of ~ 32 GPa. Foil normal $\cong [001]$. Dark-field images were taken with the electron beam $\sim 5^\circ$ off [001] in the transmission electron microscope.

from Fig. 6, the dislocation density can be expressed as a function of pressure (Fig. 15). The black, white and half-black/half-white points indicate structures consisting of purely dislocations, cellular dislocation structures and cellular dislocations with twinning, respectively [20,36].

3.5.1.1. Homogenous dislocation generation [38,39,43].

Fig. 16 shows a schematic of the shock front propagating down a bcc crystal with orientation [100]. Two configurations are shown: {110} and {112} slip planes. In Fig. 16a, four of the six {110} planes have equal Schmid factors and are shown as sides of the pyramid. Dislocation loops nucleated on these planes are shown. Their Burgers vectors are $\langle 111 \rangle$ and are parallel to the slip plane intersections. For the {112} slip planes, the Burgers vectors bisect the intersections. The calculations below use the recently revised equations [43] for homogeneous nucleation.

From Fig. 17 [43], the dislocation density, ρ , is expressed by the distance along the front and perpendicular to the front of the dislocations:

$$\rho = \frac{2}{d_2 h}$$

where d_2 is the dislocation spacing along the front obtained directly from hydrostatic compression of the lattice and h is obtained as the spacing between nucleation events perpendicular to the shock front. Two cases are considered: stationary and moving dislocations.

The spacing between dislocation planes, h , was calculated [9,43] as

$$h = \frac{0.8(1-\nu)}{\pi^2 b} d_2^2 \quad (1)$$

where b is the Burgers vector. If the dislocations are assumed to move under the effect of the applied shear stress at a velocity v_d , the spacing between sequential homogeneous loop generation events is h_2 . Under the influence of the high residual stresses, they try to “catch up” with the shock front. This results in an increase in the spacing between dislocation arrays from h to h_2 , given in Eq. (2):

$$h_2 = h \left[1 + \frac{kv_d}{U_s} \right] \quad (2)$$

where U_s is the shock-wave velocity and k is an orientation factor. When $v_d = 0$, h_2 reduces to h . When the dislocation velocity equals the shear wave velocity v_s (our maximum

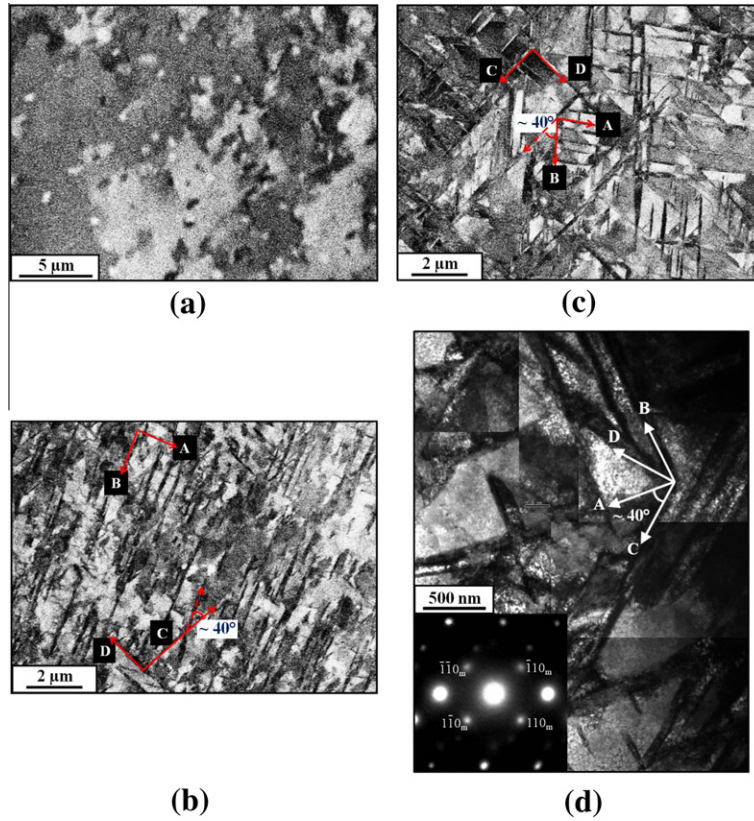


Fig. 13. Twins imaged by SEM–BSE (20 kV) in [001] Ta at $E_{\text{Laser}} = 606$ J; (a) front surface of slice 1 ($\sim 186 \mu\text{m}$ from the laser shock surface); (b) polished out $\sim 42 \mu\text{m}$ depth from the front surface of slice 1 to where twins and the deformation microstructure first become visible ($\sim 228 \mu\text{m}$ from laser shock surface); (c) back surface of slice 1 ($\sim 590 \mu\text{m}$ from the laser shock surface). All images are post-processed by inversion. (d) TEM image from FIB “bottom” ($\sim 202 \mu\text{m}$ from the laser shock surface).

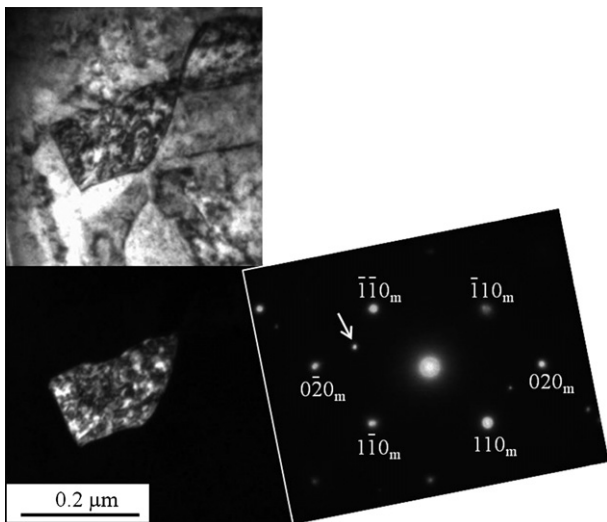


Fig. 14. ω (hexagonal) phase was observed in foil “Bottom” marked in Fig. 10(a). A bright-field and a dark-field TEM image, and the corresponding selected area diffraction pattern. ω phase was lightened at an additional spot, as marked by an arrow. Dark-field images were taken with two electron beam conditions $\sim 5^\circ$ off [001] in the transmission electron microscope.

assumed velocity for dislocation motion), h_2 reaches a maximum:

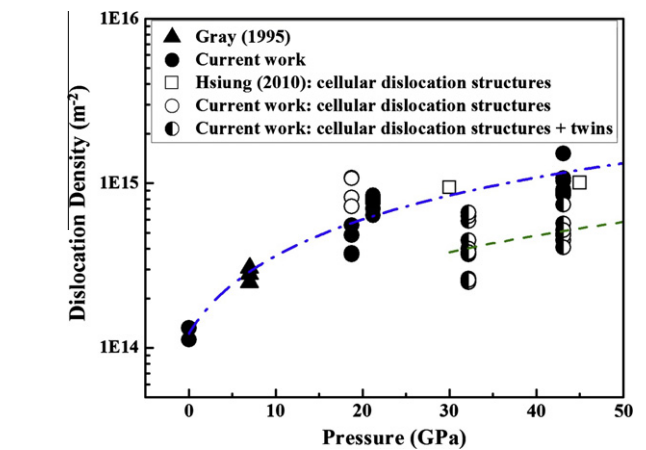


Fig. 15. Dislocation density calculated from TEM results. Black points reveal the dislocation density when only dislocations are observed. White points correspond to cellular dislocation structures. Half-black/half-white points correspond to dislocation structures with concurrent twinning [20,36].

$$h_2 = h \left[1 + \frac{kv_s}{U_s} \right] \quad (3)$$

The expression connecting the dislocation density, ρ , to the specific volume, V , for stationary dislocation is:

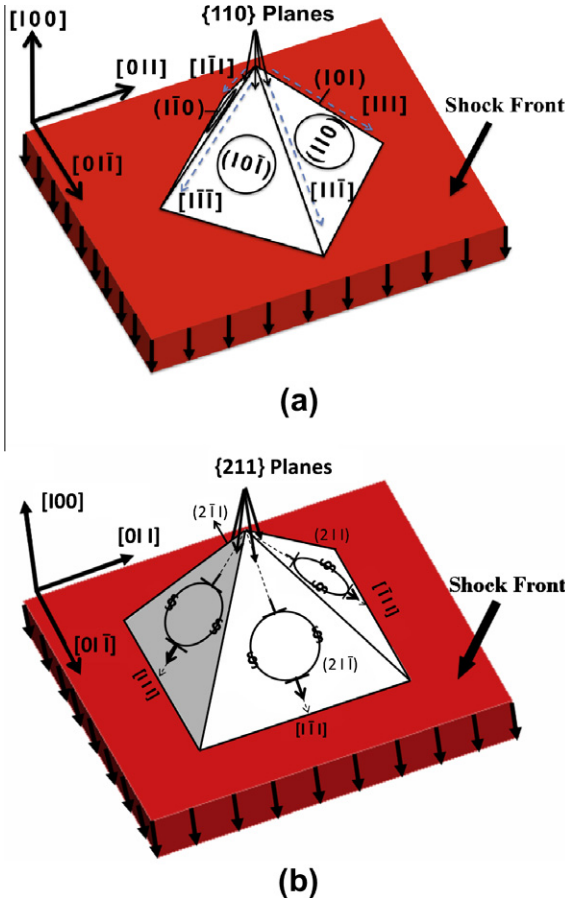


Fig. 16. Schematic representation of shear loops nucleating at (a) {110} and (b) {211} planes in shock compression along [100].

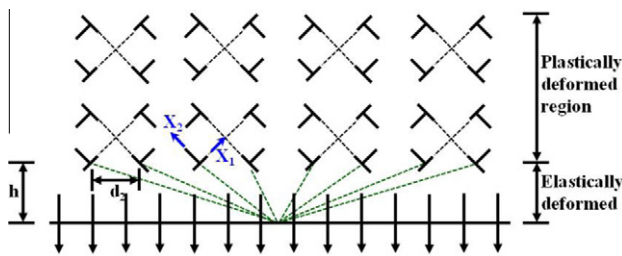


Fig. 17. Stress due to dislocations on a reference point 0 at the shock front [43].

$$\rho = \frac{2\pi^2}{0.8(1-\nu)k^3b^2} \left(\frac{V}{V_0}\right)^{-2/3} \left[1 - \left(\frac{V}{V_0}\right)^{1/3}\right]^3 \quad (4)$$

where k is an orientation parameter, ν is Poisson's ratio, and V_0 and V are the initial and compressed specific volumes of the lattices. The specific volume is, in turn, related to the pressure through the Rankine–Hugoniot relationship [44]:

$$P = \frac{C_0^2(1 - V/V_0)}{V_0[1 - S(1 - V/V_0)]^2} \quad (5)$$

where C_0 is the sound velocity, and S is a material parameter. Solving Eqs. (4) and (5) by assigning different values

$V/V_0 < 1$, one obtains the dislocation density as a function of pressure, as shown in Fig. 18a. The predictions based on the two values of h (for stationary dislocations $v_d = 0$ and for dislocations moving at the shear sound velocity $v_d = v_s$) are used in modeling dislocation density and compared with experimental results from three sources in Fig. 18a. The calculated dislocation densities are orders of magnitude higher than the values measured on recovery samples. However, it should be mentioned that, at this juncture, the model does not incorporate either relaxation during the shock nor the additional defect motion and annihilation during the rarefaction (unloading) portion of the shock pulse. This will be further developed in the future. Molecular dynamics calculations by Jarmakani et al. [12] have shown that the homogeneous generation mechanism gives values, for nickel and copper, that are comparable with the predictions of the homogeneous dislocation generation model. Upon unloading, the majority of the dislocations are annihilated in the molecular dynamics calculations.

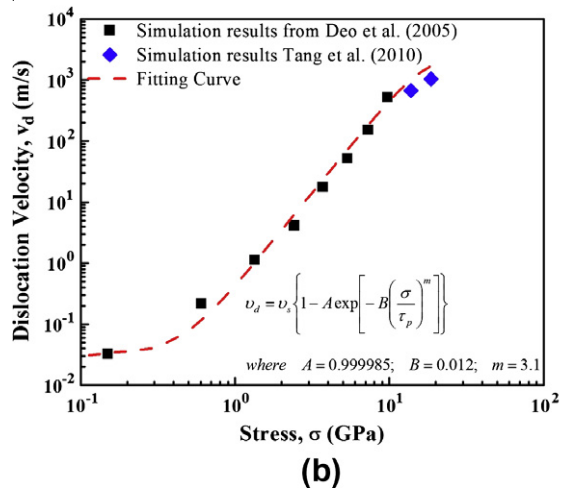
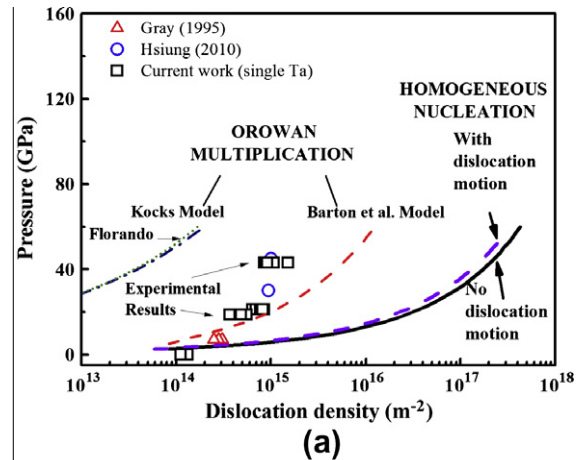


Fig. 18. (a) Residual dislocation density as a function of shock pressure for tantalum; comparison of calculated values (lines) with experimental measurements (symbols); (b) dislocation velocity as a function of stress from MD simulations. The dashed curve is a fit to the simulation results.

3.5.1.2. *Orowan dislocation multiplication.* The alternative to homogeneous dislocation generation at the front is the activation of conventional sources and an increase in dislocation density through multiplication of dislocations. The classic Orowan equation has the form:

$$\gamma = Mb\rho\ell \quad (6)$$

where $M = 3.08$ is the Taylor factor, $b = 2.86 \times 10^{-8}$ cm is the Burgers vector, ρ is the mobile dislocation density and ℓ is the mean distance traveled by a dislocation. Taking the time derivative,

$$\dot{\gamma} = \frac{d\gamma}{dt} = Mb\rho\frac{\partial\ell}{\partial t} + Mb\ell\frac{\partial\rho}{\partial t} = Mb(\rho v_d + \ell\dot{\rho}) \quad (7)$$

In order to estimate the dislocation velocity, v_d , molecular dynamics simulation results from Deo et al. [45] and Tang et al. [37] were used. The computed results were fit to the following equation:

$$v_d = v_s \left\{ 1 - A \exp \left[-B \left(\frac{\sigma}{\tau_p} \right)^m \right] \right\} \quad (8)$$

where A , B and m are parameters. The stress σ is normalized to the Peierls stress, τ_p , estimated to be $\tau_p = 3.76$ GPa [37]. Eq. (8) predicts a maximum velocity equal to the shear wave velocity ($v_s = 2,039$ m/s). The predictions from the molecular dynamics were fitted into Eq. (8) and are shown in Fig. 18b. The following fitting parameters were used: $A = 0.999985$, $B = 0.012$ and $m = 3.1$.

The relationship between pressure and strain rate in shock compression was obtained by Furnish et al. [16] for tantalum by passing a line through two experimental points. In Fig. 19, a Swegle–Grady equation ($P \propto \dot{\epsilon}^{1/4}$) is passed through these points, providing the relationship:

$$\dot{\epsilon} = 27.34 \times 10^{-36} \times P_{shock}^4 \quad (9)$$

where P is expressed in Pa and the strain rate is in s^{-1} . In laser compression, one has a state of uniaxial strain. Thus:

$$\tau = \frac{\sigma - \sigma_2}{2} = \frac{1 - 2\nu}{2(1 - \nu)} \sigma \quad (10)$$

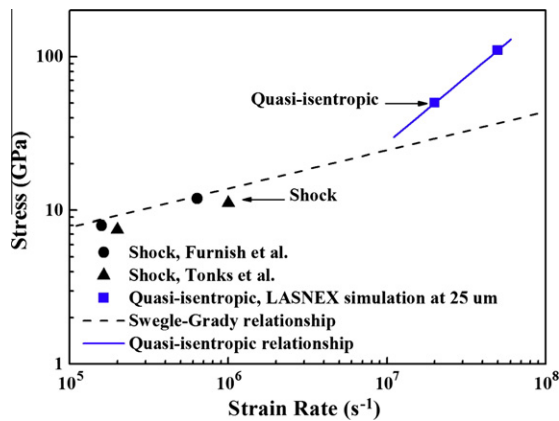


Fig. 19. Swegle–Grady relationship for Ta: $\dot{\epsilon} = 27.34 \times 10^{-36} \times P_{shock}^4$ [19], where P_{shock} is in units of Pa and $\dot{\epsilon}$ is in s^{-1} ; strain rate data within the isentropically loaded layer are also presented [16,19,64], with a Swegle–Grady relationship for Ta of $\dot{\epsilon} = 2.14 \times 10^{-31} \times P^{1.16}$.

$$G\gamma = \frac{1 - 2\nu}{2(1 - \nu)} \varepsilon E \frac{(1 - \nu)}{(1 + \nu)(1 - 2\nu)} = \frac{\varepsilon E}{2(1 + \nu)} = G\varepsilon \quad (11)$$

and thus $\gamma = \varepsilon$, where τ is the shear stress, σ is the normal stress, σ_2 is the normal stress in the transverse direction, ν is Poisson's ratio, G is the shear modulus, γ is the shear strain, ε is the normal strain and E is Young's modulus. Thus, $\dot{\gamma} = \dot{\varepsilon}$ is also used.

The rate of change in dislocation density $\dot{\rho}$ is obtained from the rate of generation, $\dot{\rho}_{gen}$, and the rate of annihilation of dislocations, $\dot{\rho}_{ann}$:

$$\dot{\rho} = \dot{\rho}_{gen} + \dot{\rho}_{ann} \quad (12)$$

The evolution of dislocation density was calculated using two expressions:

In Barton et al.'s [46] analysis, it is expressed as:

$$\dot{\rho} = (H\rho - D\rho^2)v_d = R \left(1 - \frac{\rho}{\rho_{sat}(\dot{\epsilon}_p)} \right) \dot{\epsilon}_p \quad (13)$$

$$\text{where } \rho_{sat}(\dot{\epsilon}_p) = \rho_{s0} \left(\frac{\dot{\epsilon}_p}{\dot{\epsilon}_N} + S_0 \right)^n \quad (14)$$

where ρ_{sat} is the saturation dislocation density; H , D , R , S_0 and n are parameters.

Inserting Eqs. (13) and (14) into Eq. (7):

$$\dot{\gamma} = Mbv_d\rho + Mbv_d t R \dot{\epsilon}_p - Mbv_d t R \dot{\epsilon}_p \frac{\rho}{\rho_{sat}(\dot{\epsilon}_p)} \quad (15)$$

$$\rho = \rho(\dot{\epsilon}_p, v_d) = \rho(P) = \frac{\dot{\epsilon}_p - Mbv_d t R \dot{\epsilon}_p}{\left(Mbv_d - \frac{Mbv_d t R \dot{\epsilon}_p}{\rho_{sat}(\dot{\epsilon}_p)} \right)} \quad (16)$$

The following parameters from Barton et al. [46] for tantalum are used: $R = 10^{18} m^{-2}$, $\rho_{s0} = 1.1266 \times 10^{11} m^{-2}$, $\dot{\epsilon}_N = 1 s^{-1}$, $S_0 = 650$ and $n = 0.59$. The value of R used here is a factor of 10 larger than that given by Barton et al. [46] in order to predict results that approximate the observations by TEM reasonably. Applying Eqs. (8) and (9) to Eq. (16), one obtains a relationship between dislocation density and pressure. The result is plotted in Fig. 18a. It can be seen that the curve, marked "Barton et al.", predicts densities that are fairly close to the observed residual densities at lower pressures. At higher pressures, twinning accommodates part of the strain and the experimental dislocation densities are lower than predicted values. In a more general relationship, the overall strain based on Orowan equation has been expressed as

$$\gamma = \begin{cases} Mb\rho_{\perp}l & \text{if } \dot{\gamma} < \dot{\gamma}_{threshold} \\ Mb\rho_{\perp}l + f_T\gamma_T & \text{if } \dot{\gamma} > \dot{\gamma}_{threshold} \end{cases}$$

where ρ_{\perp} is the dislocation density, f_T is the twin fraction, γ_T is the twin strain ($= 0.707$ in bcc [47]) and $\dot{\gamma}_{threshold}$ is the threshold strain rate at which the slip–twinning transition occurs. For a strain rate below the threshold, the dislocation density increases with increasing strain as a result of increasing pressure. Above the threshold strain rate, part of the strain is accommodated by dislocations through Orowan and part through twinning.

In Kocks's model [48], the dislocation density rate $\dot{\rho}$ can be expressed as

$$\dot{\rho} = (k_1 \rho^{1/2} - k_2 \rho) \dot{\gamma} \quad (17)$$

where k_1 and k_2 are experimentally determined parameters, and $\dot{\gamma}$ is the shear strain rate ($= \dot{\epsilon}$ for uniaxial strain, Eq. (11)). The first term represents dislocation generation and the second, dislocation annihilation. The difference with the Barton et al. [46] model is in the exponents of the dislocation generation ($1/2$ vs. 1) and annihilation (1 vs. 2) terms. Two methods were used to estimate the parameters k_1 and k_2 in the dislocation density evolution:

Method 1: The saturation dislocation density is defined by: $\rho = \rho_{sat}$, $\dot{\rho} = 0$. Using the approach from Barton et al. [46]:

$$\left(\frac{k_1}{k_2}\right)^2 = \rho_{sat} = \rho_{sat}(\dot{\epsilon}_p) = \rho_{s0} \left(\frac{\dot{\epsilon}_p}{\dot{\epsilon}_N} + S_0\right)^n \quad (18)$$

$$\begin{aligned} \rho &= (\rho^{1/2})^2 \\ &= \left(\frac{-Mbv_d t \dot{\gamma} k_1 \pm \sqrt{(Mbv_d t \dot{\gamma} k_1)^2 - 4(Mbv_d - Mbv_d t \dot{\gamma} k_2)(-\dot{\gamma})}}{2(Mbv_d - Mbv_d t \dot{\gamma} k_2)}\right)^2 \end{aligned} \quad (19)$$

where we set $k_2 = 1 \times 10^{-5}$.

Method 2: Florando et al. [49] recently presented the parameter relationship for the dislocation evolution equation based on Kocks's [48] equation:

$$k_2 = k_{20} \left(\frac{\dot{\epsilon}_r}{\dot{\epsilon}}\right)^{1/n} \quad (20)$$

where $k_1 = 16719$, $k_{20} = 983.473$, $\dot{\epsilon}_r = 1 \text{ s}^{-1}$ and $n = 0.25$.

The predictions of Kocks [48] equation and its modification by Florando et al. [49] based on Orowan multiplication are shown in Fig. 18a. The values are considerably lower than the ones using the Barton et al. [46] equation (with the corrected value for R). The two predictions bracket the experimental results. It may be concluded that dislocation multiplication can correctly predict the evolution of dislocation density in shock compression of bcc tantalum.

The differences between the models are still an unresolved issue that needs to be addressed through a combination of experiments, analysis and molecular dynamics simulations. Two possible reasons for the differences have been identified:

- The dislocation density increases through conventional multiplication according to the Orowan equation. In this case, the strain dependence of the dislocation generation and annihilation terms followed the Barton et al. [46] model, based on Orowan multiplication. According to the discussion at the beginning of Section 3.5.1, the dislocation density

decreased as twin structures were observed at higher pressure.

- Dislocations are homogeneously nucleated but a large fraction of the dislocations generated in the shock front are annihilated during the release portion of the pulse. This was hypothesized earlier for Ni and Cu via molecular dynamics simulations [12].

3.5.2. Slip–twinning transition

Slip and twinning can be considered as competing deformation processes. This criterion enables an analysis that leads to the predicted transition between the two mechanisms. They are both determined by shear stresses acting in the slip or twin plane and in the direction of displacement (τ_s and τ_T , respectively). To a first approximation, one can establish a criterion for the dominance of one deformation regime by using the transition in which the shear stresses are equal:

$$\tau_s = \tau_T \quad (21)$$

During shock compression, in the elastic loading stage one can relate the maximum shear stress to the stresses aligned with (σ_{xx}) and perpendicular to (σ_{yy}) the propagation direction (e.g., Stirk et al. [50]):

$$\tau = \frac{1}{2}(\sigma_{xx} - \sigma_{yy}) = \frac{1-2\nu}{2(1-\nu)} \sigma_{xx} \quad (22)$$

where ν is Poisson's ratio ($=0.34$ for Ta). Assuming that, to a first approximation, Poisson's ratio is independent of pressure, one has: $\tau = 0.24\sigma_{xx}$. Thus, there is a direct relationship between the normal stress (that is directly related to the pressure, P) and the shear stress prior to plastic deformation.

The slip–twinning analysis proposed by Meyers et al. [51] has been extended successfully to the shock compression domain [10,11,52]. Meyers et al. [11] and Jarmakani et al. [52] have developed constitutive descriptions for the slip–twinning transition for copper and nickel, respectively. In the calculations presented here, this treatment is extended to a bcc metal, tantalum, as done previously by Murr et al. [19]. The effects of strain rate on slip can be expressed by the Zerilli–Armstrong equation for bcc metals [15]:

$$\tau_S = \tau_S^* + C_2 e^{-C_3 T} \dot{\epsilon}^{C_4 T} + k_S d^{-1/2} \quad (23)$$

where τ_S is slip stress, τ_S^* is athermal stress and d is the grain size. C_1 , C_2 , C_3 , C_4 and k_S are parameters that have been established for tantalum. The twinning stress, τ_T , has been expressed by Armstrong and Worthington [53] as:

$$\tau_T = \tau_0 + m \left(\frac{Gb}{C_1}\right)^{1/2} \left[\frac{U^*}{RT} \ln \frac{\dot{\epsilon}}{\dot{\epsilon}_0}\right]^{1/4} d^{-1/2} \quad (24)$$

where τ_0 is a frictional stress, m is an orientation factor, G is the shear modulus, b is the Burgers vector, U^* is a normalized activation energy for twinning, R is the gas constant, $\dot{\epsilon}_0$ is a reference strain rate, d is the grain size, and

the exponent q varies between 4 and 8. The effect of strain rate on twinning can be neglected, to a first approximation. This can be surmised from the $1/q$ exponent in Eq. (24), where q has a large value of ~ 5 , as shown earlier by Meyers et al. [51]. Thus, the onset of twinning can be obtained by setting Eq. (23) equal to Eq. (24), following the criterion expressed in Eq. (21).

It is clear from the above discussion that, in shock compression, twinning is triggered by the shear stresses and not by the pressure. However, both are related by Eq. (22). The pressure only creates the strain rate at the front, which in turn determines the level of shear stress. Applying the Swegle–Grady equation ($P \propto \dot{\epsilon}^{1/4}$) shown in Fig. 19 ($\dot{\epsilon} = 27.34 \times 10^{-36} \times P_{shock}^4$) to Eqs. (23) and (24), one can calculate the stresses required for slip and twinning, respectively, as a function of pressure. In isentropic compression, the strain rate is significantly lower for a prescribed pressure (Fig. 19). Average strain rates were computed from the effective plastic strain and compression time calculated through LASNEX in the first 25 μm layer. The results are also shown in Fig. 19.

There is extensive prior work indicating that the twinning stress is dependent on interstitial content. Table 1 summarizes the different observations on twinning in tanta-

lum. The differences obtained by different investigators confirm this. Barrett and Bakish [54] obtained twinning by impact deformation at 77 K, but not at 273 K; their Ta had ~ 300 ppm C. On the other hand, Anderson and Bronisz [55] had a total of ~ 53 ppm of C, O, H and N impurity in their samples. They were able to twin Ta ($d = 4$ mm) at room temperature. Shock compression of polycrystalline Ta at room temperature suggests a concurrence of lower shock pressures at lower interstitial content at which twinning is observed [36,54–56]. Accordingly, the reported twinning stresses also vary with the source. Mitchell and Spitzig [18] observed twinning only in tensile tests at 4.2 K. From Mitchell and Spitzig [18], a twinning stress of 887.7 MPa (in tension) was calculated using $\{112\}\langle 111\rangle$ twin system by finding the corresponding tension on $[100]$. It should be mentioned that loading was in the center of the stereographic triangle. In contrast, the twinning stresses in tension and compression were established for loading along $[100]$ by Sherwood et al. [56]. They obtained values that varied widely, and this is explained by the twinning plane and direction. The twinning stresses in tension and compression were 370 and 755 MPa, respectively, for $[100]$ monocrystal. Thus, there is a large difference between the twinning stress in tension of Mitchell and Spitzig [18]

Table 1
Interstitial content and twinning occurrence from different investigations.

| Investigator | Interstitial (ppm) | Monocrystal/polycrystal | Twin | Temperature (K) | Tension/compression |
|---------------------------|--|---|-----------|------------------------|--|
| Bechtold [31] | 100 C 100 N | Polycrystal (47 μm) | No | 77 | Tension |
| Barrett and Bakish [54] | 300 C | Polycrystal | Yes No | 77 196 273 | Compressive impact |
| Anderson and Bronisz [55] | 20 C 8 O ₂ 15 N ₂ 10 H ₂ | Polycrystal (4 mm) | Yes | RT (298 K) | Compressive impact |
| Mitchell and Spitzig [18] | 18 C 37 O 6 N <1 H | Monocrystal [123] | Yes | 4.2 | Tension |
| Sherwood et al. [56] | 36 C 11 O 7 N 11 H | Monocrystal [100] Monocrystal [110] | Yes | 77 4.2 77 4.2 | Tension (370 MPa) Compression (755 MPa) Tension (680 MPa) Compression (350 MPa) |
| Gray and Vecchio [36] | 6 C 56 O 24 N <1 H | Polycrystal (~ 68 μm) | Yes | RT (298 K) | Compression shock (~ 20 GPa) |
| Murr et al. [19] | 70 C 60 O 10 N 4 H | Polycrystal (~ 43 μm) | Yes | RT (298 K) | Compression shock (~ 45 GPa) |
| Lu et al. (current work) | <10 C <10 O <10 N 7.6 H | Monocrystal [100] | Yes | RT (298 K) | Compression shock (~ 110 GPa) |

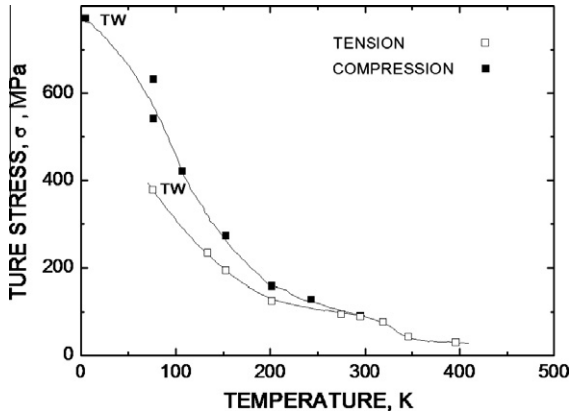


Fig. 20. Temperature dependence of the asymmetry of flow stress for slip and twinning stresses in tension and compression for tantalum with [100] orientation (from Sherwood et al. [56]) at a strain rate of $\dot{\epsilon} = 10^{-4} \text{ s}^{-1}$. TW represents the conditions at which twinning is observed.

Table 2
Zerilli–Armstrong and other modeling parameters for experimental data fitting.

| Parameters | Unit | Value |
|------------------------------------|-----------------|---------|
| T | K | 298 |
| Athermal stress | MPa | 20 |
| C_1 | N/A | 0.0005 |
| $C_2 = B_0$ | MPa | 1125 |
| $C_3 = \beta_0$ | K^{-1} | 0.00535 |
| $C_4 = \beta_1$ | K^{-1} | 0.00024 |
| Tension twin stress | MPa | 370 |
| Compression twin stress σ_0 | MPa | 755 |
| Burgers vector | nm | 0.286 |

and Sherwood et al. [56]. The experimental results by Sherwood et al. [56] are the most complete because they include tension and compression of [100] and [110] monocrystals, and therefore will be used in this analysis. The inverse trend of tension–compression asymmetry pressure between [100] and [110] is not discussed in this paper. There is a significant tension–compression asymmetry in the shear stress of bcc metals that has been extensively investigated by Vitek and co-workers [13,57–60] and Seeger [61], among others. This tension–compression asymmetry is due to dislocation core effects. The yield stress in tension is lower than in compression in [100] monocrystal; the influence gradually decreases with increasing temperature, as evident from the data of Sherwood et al. [56], plotted in Fig. 20. The compressive and tensile yield stresses are equal at 300 K. Thus, from Fig. 20, no apparent tension–compression asymmetry should be expected in our 300 K laser shock experiments. The (quasi-static and dynamic) experiments by Rittel et al. [62] and quasi-static experiments in current investigation (both in compression) were used to obtain the Z–A parameters, C_4 and C_2 , given in Table 2. Fig. 21 shows the application of the Z–A parameters in the prediction of the strain rate dependence of the flow stress. The twinning curves in tension and compression are shown in

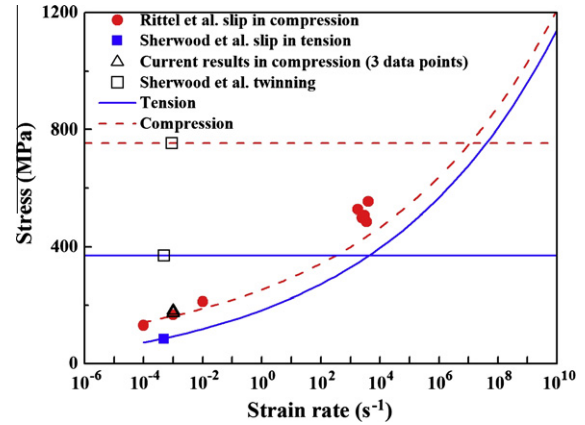


Fig. 21. Flow stress–strain rate curves for [100] single crystal Ta deformed in tension (full lines) and compression (dash lines) [62]. The twinning stresses in tension and compression (from Sherwood et al. [56]) were assumed to be independent of strain rate. The higher yield stresses at high strain rates is due to our linear extrapolation from Rittel et al.'s [62] data.

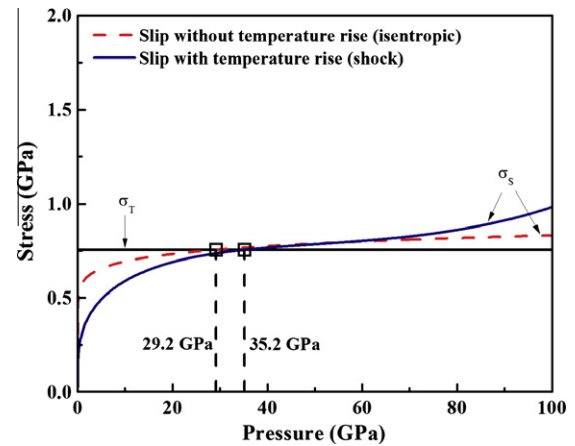


Fig. 22. Slip and twinning stress vs. shock pressure for Ta (grain size $d = 3 \text{ mm}$). The dashed curve corresponds to the isothermal case (close to isentropic compression); the solid curve includes the adiabatic shock-induced temperature rise (shock compression). The threshold ranges from 29.2 to 35.2 GPa.

the same plot, assuming no strain-rate sensitivity, due to the high value of q in Eq. (24).

The temperature rise in Ta as a function of shock pressure can be expressed as the second-order polynomial, based on the R–H equations (and on the C_0 and S values for Ta [63]):

$$T_{shock_Ta} = 1.007 \times 10^{-19} P_{shock}^2 - 1.13 \times 10^{-9} P_{shock} + 294.8 \quad (25)$$

where P_{shock} is expressed in units of Pa.

The calculated slip–twinning transition stress varies in the ~ 29 – 35 GPa range and is affected by consideration of the thermal rise in specimens during loading, i.e. isothermal (for quasi-isentropic) vs. adiabatic compression (for shock), as shown in Fig. 22. In our present study, twinning

is observed above a 32 GPa pressure threshold for experiments performed at 300 K. Thus, considering the various approximations and assumptions of the model, the predictions match the experimental results fairly well.

4. Summary and conclusions

1. Tantalum monocrystals were subjected to laser compression utilizing an experimental set-up that provides quasi-isentropic loading for the first ~ 40 μm depth; after this, the rise time of the pulse decreases and becomes a shock discontinuity.
2. The defects generated by the laser pulse were characterized by transmission and scanning electron microscopy, and are composed of dislocations at low pressures, and mechanical twins and a displacive phase transformation at higher pressures.
3. The dislocation density increased with the proximity to the energy deposition surface. The experimentally observed dislocation density was compared with calculations based on homogeneous dislocation generation and Orowan dislocation multiplication.
4. The homogeneous dislocation generation mechanism predicts results that are higher by orders of magnitude than the experimentally measured densities. These results are consistent with earlier investigations on copper (an fcc metal) [9].
5. The lower dislocation density observed experimentally might be due to two reasons: (a) dislocations are not homogeneously nucleated but rather increase their density as a result of movement, interaction and multiplication from existing sources; (b) a significant fraction of the dislocations generated homogeneously in shock compression are annihilated upon release.
6. An analysis based on the Orowan mechanism of multiplication and involving two forms of dislocation generation and annihilation terms (Barton et al. [46] and Kocks [48]) was applied and enabled the prediction of dislocation densities as a function of pressure. The Barton et al. [46] analysis predicted dislocation densities that are consistent with experimental results at lower pressures but higher than the experimental results at higher pressure. The difference may come from the effect of mechanical twins accommodating part of the strain.
7. In the proximity of the energy-deposition surface, as the shock pressure increases, the dislocations give way to mechanical twinning as the principal deformation mode. The experimentally obtained slip–twinning threshold stress is ~ 32 –43 GPa. Calculations involving constitutive equations for slip and twinning and the Swegle–Grady equation predict a pressure ~ 29 –35 GPa range, consistent with experimental results.
8. The ω -phase was observed at a peak pressure of ~ 68 GPa. From the current results and Hsiung and Lassila's [22] experiments, it can be concluded that the experimentally obtained phase transformation pressure

is ~ 43 –68 GPa. This is higher than the twinning threshold stress.

Acknowledgements

This research is funded by a UC Research Laboratories Grant (09-LR-06-118456-MEYM) and a National Laser Users Facility (NLUF) Grant (PE-FG52-09NA-29043). We thank T. Remington for yield stress measurement, C.T. Wei for help with the manuscript preparation, Rain Luo for profilometry measurement, Dr. Fabienne Gregori for her hospitality at the Université Paris Nord and for transmission electron microscopy, and Dr. Y. Tang for overall assistance. Electron microscopy was conducted at the SHaRE User Facility, which is sponsored at Oak Ridge National Laboratory by the Division of Scientific User Facilities, US Department of Energy. We acknowledge the use of the UCSD Cryo-Electron Microscopy Facility, which is supported by NIH grants to Dr. Timothy S. Baker and a gift from the Agouron Institute to UCSD.

References

- [1] Askaryan GA, Prokhorov AM, Chanturiya GF, Shipulo GP. *Sov Phys JETP-USSR* 1963;17:1463.
- [2] Safonov AN, Grigor'yants AG, Makusheva NA, Sergeev AV. *Elektronnaya Obrabotka Materialov* 1984;1:26.
- [3] Gureyev DM, Zolotarevsky AV, Zaikin AE. *J Mater Sci* 1991;26:4678.
- [4] White RM. *Inst Radio Eng Trans Instrum* 1962;I-11:294.
- [5] White RM. *J Appl Phys* 1963;34:2123.
- [6] Bell CE, Landt JA. *Appl Phys Lett* 1967;10:46.
- [7] Panarell E, Savic P. *Can J Phys* 1968;46:183.
- [8] Skeen CH, York CM. *Appl Phys Lett* 1968;12:369.
- [9] Meyers MA, Gregori F, Kad BK, Schneider MS, Kalantar DH, Remington BA, et al. *Acta Mater* 2003;51:1211.
- [10] Schneider MS, Kad B, Kalantar DH, Remington BA, Kenik E, Jarmakani H, et al. *Int J Impact Eng* 2005;32:473.
- [11] Meyers MA, Schneider MS, Jarmakani H, Kad B, Remington BA, Kalantar DH, et al. *Metall Mater Trans A* 2008;39A:304.
- [12] Jarmakani HN, Bringa EM, Erhart P, Remington BA, Wang YM, Vo NQ, et al. *Acta Mater* 2008;56:5584.
- [13] Groeger R, Vitek V. *Philos Mag* 2009;89:3163.
- [14] Hobart RJ. *Appl Phys* 1965;36:1944.
- [15] Zerilli FJ, Armstrong RW. *J Appl Phys* 1990;68:1580.
- [16] Furnish MD, Chhabildas LC, Steinberg DJ. *Shock Comp Condens Matter AIP Conf Proc* 1994;309:1099.
- [17] Thissell WR, Zurek AK, Tonks DL, Hixson RS. *Shock Comp Condens Matter AIP Conf Proc* 2000;505:451.
- [18] Mitchell TE, Spitzig WA. *Acta Metall* 1965;13:1169.
- [19] Murr LE, Meyers MA, Niou CS, Chen YJ, Pappu S, Kennedy C. *Acta Mater* 1997;45:157.
- [20] Hsiung LL. *J Phys Condens Matter* 2010;22:385702.
- [21] Hsiung LM, Lassila DH. *Scr Mater* 1998;38:1371.
- [22] Hsiung LM, Lassila DH. *Acta Mater* 2000;48:4851.
- [23] Meyers MA. *Dynamic behavior of materials*. New York: John Wiley & Son; 1994.
- [24] Marian J, Cai W, Bulatov VV. *Nat Mater* 2004;3:158.
- [25] Bringa M, Rosolankova K, Rudd RE, Remington BA, Wark JS, Duchaineau M, et al. *Nat Mater* 2006;5:805.
- [26] Kalantar DH, Belak JF, Collins GW, Colvin JD, Davies HM, Eggert JH, et al. *Phys Rev Lett* 2005;95:075502.

- [27] Edwards J, Lorenz KT, Remington BA, Pollaine S, Colvin J, Braun D, et al. *Phys Rev Lett* 2004;92:075002.
- [28] http://www.lle.rochester.edu/omega_facility/omega/.
- [29] http://www.lle.rochester.edu/media/about/documents/nluf_users_guide.pdf.
- [30] Lorenz KT, Edwards MJ, Jankowski AF, Pollaine SM, Smith RF, Remington BA. *High Energy Density Phys* 2006;2:113.
- [31] Bechtold JH. *Acta Metall* 1955;3:249.
- [32] Ferriss DP, Wulff J, Rose RM. *Trans Metall Soc AIME* 1962;224:584.
- [33] Cheung KS, Yip S. *Modell Simul Mater Sci Eng* 1994;2:865.
- [34] Murr LE. *Scr Metall* 1978;12:201.
- [35] Zhou JK, Hsiung LL, Chau R, Saw CK. *Shock Comp Condens Matter AIP Conf Proc* 2007;955:677.
- [36] Gray GT, Vecchio KS. *Metall Mater Trans A* 1995;26:2555.
- [37] Tang Y, Bringa EM, Remington BA, Meyers MA. *Acta Mater* 2011;59:1354.
- [38] Meyers MA. *Strength of metals and alloys*. New York: Pergamon; 1979.
- [39] Meyers MA. *Scr Metall* 1978;12:21.
- [40] Smith CS, Guttman L. *Trans Am Inst Min Metall Eng* 1953;197:81.
- [41] Bailey JE, Hirsch PB. *Philos Mag* 1960;5:485.
- [42] Ham RK. *Philos Mag* 1961;6:1183.
- [43] Meyers MA, Jamarkani H, Bringa E, Remington B. In: Hirth JP, Kubin L, editors. *Dislocation in solids*, vol. 15. Amsterdam: Elsevier; 2009.
- [44] Armstrong RW, Elban W. In: Hirth JP, Kubin L, editors. *Dislocations in Solids*. Amsterdam: Elsevier; 2004.
- [45] Deo CS, Srolovitz DJ, Cai W, Bulatov VV. *J Mech Phys Solids* 2005;53:1223.
- [46] Barton NR, Bernier JV, Becker R, Arsenlis A, Cavallo R, Marian J, et al. *J Appl Phys* 2011;109:073501.
- [47] Meyers MA, Chawla KK. *Mechanical behavior of materials*. Cambridge: Cambridge University Press; 2008.
- [48] Kocks UF. *J Eng Mater Technol* 1976;98:76.
- [49] Florando JN, McNaney J, Hsiung L, Barton NR, Kumar M. Presentation at TMS 140th annual meeting, San Diego, 27 February–3 March 2011.
- [50] Stirk SM, Millet JCF, Bourne NK, Whiteman G, Park NT. *Shock Comp Condens Matter AIP Conf Proc* 2009;1123–6.
- [51] Meyers MA, Voehringer O, Lubarda VA. *Acta Mater* 2001;49:4025.
- [52] Jarmakani H, Wang YM, Bringa E, Meyers MA. *Shock Comp Condens Matter AIP Conf Proc* 2007;955:239.
- [53] Armstrong RW, Worthington PJ. *Metallurgical effects at high strain rates*. New York: Plenum; 1973.
- [54] Barrett CS, Bakish R. *Trans Am Inst Min Metall Eng* 1958;212:122.
- [55] Anderson RW, Bronisz SE. *Acta Metall* 1959;7:645.
- [56] Sherwood PJ, Guiu F, Kim HC, Pratt PL. *Can J Phys* 1967;45:1075.
- [57] Duesbery MS, Vitek V. *Acta Mater* 1998;46:1481.
- [58] Groeger R, Bailey AG, Vitek V. *Acta Mater* 2008;56:5401.
- [59] Groeger R, Racherla V, Bassani JL, Vitek V. *Acta Mater* 2008;56:5412.
- [60] Groeger R, Vitek V. *Acta Mater* 2008;56:5426.
- [61] Seeger A. *Z Metallkd* 2002;93:760.
- [62] Rittel D, Silva ML, Poon B, Ravichandran G. *Mech Mater* 2009;41:1323.
- [63] Meyers MA, Murr LE. *Shock waves and high-strain-rate phenomena in metals*. New York: Plenum Press; 1981.
- [64] Tonks DL, Hixson RS, Johnson JN, Gray III GT. *Shock Comp Condens Matter AIP Conf Proc* 1994;309:997.